Carbon Nanotubes for Quantum Dot Photovoltaics with Enhanced Light Management and Charge Transport

Yujiro Tazawa[†], *Severin N. Habisreutinger*[‡§], *Nanlin Zhang*[†], *Daniel A.F. Gregory*[†], *Gabriel Nagamine*[⊥], *Sameer V. Kesava*[‡], *Giulio Mazzotta*[‡], *Moritz Riede*[‡], *Lazaro A. Padilha*[⊥], *Robin J. Nicholas*[‡], *Andrew A.R. Watt**[†]

† Department of Materials, University of Oxford, 16 Parks Road Oxford OX1 3PH, United Kingdom

‡ Department of Physics, University of Oxford, Clarendon Laboratory, Parks Road, Oxford OX1 3PU, United Kingdom

§ Chemistry & Nanoscience Center, National Renewable Energy Laboratory, 15013 Denver West Parkway, Golden, Colorado 80401, United States

⊥ Instituto de Física "Gleb Wataghin", Universidade Estadual de Campinas, Rua Sérgio Buarque de Holanda, 777, Campinas, SP, 13083-859, Brazil

*E-mail: andrew.watt@materials.ox.ac.uk

KEYWORDS. Colloidal quantum dots, photovoltaics, single-walled carbon nanotube, hole transport layer, charge carrier transfer, optical spacer effect

ABSTRACT. Colloidal quantum dot (CQD) based photovoltaics are an emerging low-cost solar cell technology with power conversion efficiencies exceeing 10%, i.e. high enough to be interesting for commercialisation. Well-controlled and understood charge carrier transport through the device stack is required to make the next step in efficiency improvements. In this paper, polymer wrapped single-walled carbon nanotubes (SWNTs) films embedded in an insulating polymethylmethacrylate (PMMA) matrix and capped by a thermally evaporated Au electrode are investigated as a composite hole transport layer and optical spacer. Employing transient absorption spectroscopy we show that the SWNTs enhance the charge transfer rate from CQD to CQD, ZnO, or SWNT. In order to pinpoint the underlying mechanism for the improvement, we investigate the energetics of the junction by measuring the relative alignment of the band edges, using Kelvin probe and cyclic voltammetry. Measuring the external quantum efficiency and absorption we find that the improvement is not mainly from electronic improvements but from enhanced absorption of the CQD absorber. We demonstrate experimentally and theoretically, by employing a transfer-matrix model that the transparent PMMA matrix acts as an optical spacer which leads to an enhanced absorption in the absorber layer. With those electronic and optical enhancements, an efficiency of the PbS CQD solar cells improved from 4.0% to 6.0%.

MAIN TEXT

Third generation solar cells, such as those based upon PbS colloidal quantum dot (CQD), present the possibility to build robust, low-cost photovoltaic devices using facile solution processing.[1,2] One of the most promising aspects of CQD photovoltaics is that they have the potential to break the Shockley-Queissier limit through multi-exciton generation.[3,4] Quantum-size effects[5] and surface chemical modifications have been shown to be effective means to finely tune the energy level position, bandgap, and p-type or n-type electronic properties of CQD.[6] Surface chemical modifications have been demonstrated to alter charge carrier mobility,[7] and to reduce trap states.[8-10] The use of combinations of different ligands in different layers of photovoltaic devices has led to significant improvements in open-circuit voltage (V_{oc}) and fill factor (FF).[11,12]

Efficient charge-selective layers adjacent to absorber layers reduce voltage losses at the contacts and are also essential for reducing charge carrier recombination by selectively block the undesirable photogenerated electrons towards cathode or holes towards anode which cause the charge carrier recombination.[13] Furthermore, some of these charge transport layers reduce the probability of pin-holes in the device.[14–18] To date, efficiencies of CQD photovoltaics have not

exceeded values of 14 %[19] due to radiative and non-radiative recombination losses,[20] the misalignment of electronic levels at the semiconductor-semiconductor and metal-semiconductor interfaces,[21] and optical interference effects.[22,23] To overcome some of these limitations, and to improve the charge carrier transport from light absorber to the electrodes, this paper investigates the use of single walled carbon nanotubes (SWNT), as hole-selective contact. SWNTs are well-known for their mechanical and chemical stability[24] and, in particular, for their high electrical conductivity.[25,26] SWNTs can have metallic or p-type semiconducting characteristics depending on their structure, namely their diameter and symmetry of the two-dimensional carbon lattice.[27,28] In recent years, a number of reports have shown that by wrapping SWNTs with conjugated polymers, processing challenges such as dispersibility and bundle formation can be overcome, thus opening the possibility to make use of the exceptional charge transport characteristics of SWNTs in different photovoltaics such as organic and perovskite solar cells.[29–32]

RESULTS and DISCUSSION

Device architecture and performance

In this paper, we use SWNTs which are wrapped in a monolayer of poly(3-hexylthiophene-2,5-

diyl (P3HT) and coated by an insulating poly(methylmethacrylate) (PMMA) matrix as selective hole transporting layers at the interface between the PbS absorber and the top Au electrode. The power-conversion efficiency of the CQD-SWNT devices significantly outperforms that of control devices without the SWNT layer. We attribute the improvement in PCE to synergistic effects of the SWNT-PMMA layer as charge-collection and optical spacer layer which leads to enhanced charge carrier extraction and better light-harvesting.

Figure 1a shows a schematic of the device examined here, where all functional layers of the photovoltaic device are solution processed except for sputter coated indium tin oxide (ITO) electrodes on glass substrates and thermally evaporated gold as top electrode. On top of the ITO an electron transporting zinc oxide layer, prepared by a sol-gel method,[33] is deposited and followed by a CQD absorber layer which is composed of PbS CQD stabilized by methylammonium iodide. This iodide ligand has been shown with higher charge carrier mobilities. Control devices have a direct contact between PbS CQD layer and the Au hole contact. For the SWNT devices, the hole transport layer is processed by sequential spincoating first the SWNTs from chloroform followed by a PMMA layer from chlorobenzene leading to an embedding of the SWNT in a PMMA matrix. Finally, 100 nm of Au were thermally evaporated to form the top-contact.

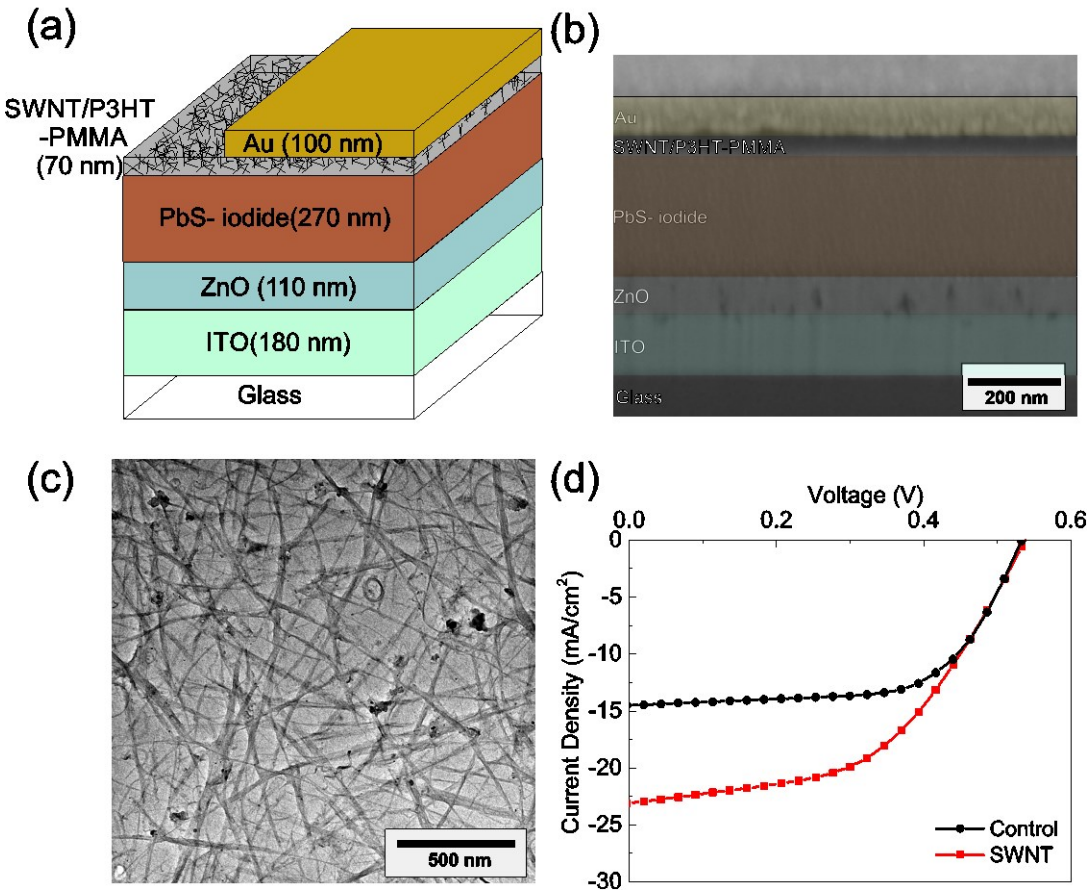

Figure 1. (a) Device structure of SWNT PbS CQD solar cells consists of ITO anode, ZnO, PbS-iodide, SWNT/P3HT in PMMA matrix, and Au cathode. (b) FIB-SEM micrograph of cross-section of the device with SWNT/P3HT-PMMA. (c) TEM micrograph of spin-coated SWNT/P3HT. (d) J-V curves for champion PbS CQD PV devices with SWNT/P3HT in PMMA (SWNT: red line with square symbols), and without SWNT/P3HT in PMMA (Control: black line with circle symbols).

A focused ion beam scanning-electron microscope (FIB-SEM) image of the device (figure 1b) shows its cross-section of the SWNT device, and a transmission electron microscope (TEM) image in figure 1c illustrates the size and aspect ratio of the SWNTs. Champion devices' current-voltage curves are shown in figure 1d, comparing the performance with and without the SWNT

layer. A statistical comparison of device performance is shown in Fig 2a-d. There is an overall improvement in the PCE by around 2.0% absolute when the SWNTs are included. This enhancement arises from significant improvements (>50%) in the short-circuit current (J_{sc}). However, FF is slightly worse for the SWNT devices (~10% relative loss) with a small improvement in V_{oc}. FF which gets lower with applying SWNT/P3HT in PMMA matrix is discussed with intensity dependence of V_{oc} in the supporting information (see figure S4). A series of experiments were performed to understand the mechanism of the observed effects.

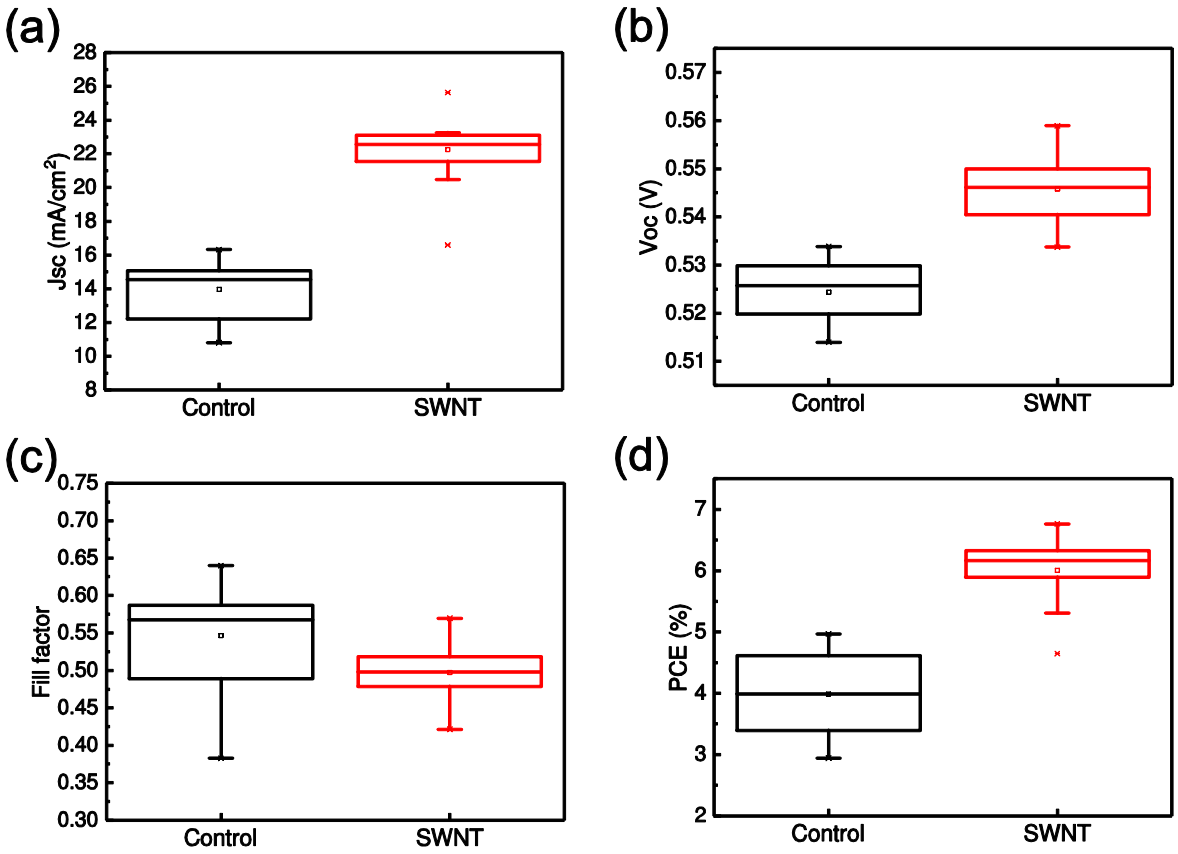

Figure 2. (a) J_{sc}, (b) V_{oc}, (c) FF, and (d) PCE of devices without SWNT/P3HT (Control in figure), and devices with SWNT/P3HT (SWNT in figure) at day 2 of storage in the air. Square symbols at the middle of the boxes are mean values. The upper lines, middle lines, lower lines of the boxes are representing 75 percentile, median, and 25 percentile respectively. Whiskers cover maximum and minimum values excluding outlier that is off from upper lines or lower lines. The reported mean values and percentiles for all parameters were calculated from a sample of 12 devices.

Charge transfer

In a photovoltaic device in which the terminals are connected without a load, the J_{sc} corresponds to the number of photogenerated charge carriers which are successfully extracted into the external circuit having evaded both radiative and non-radiative recombination processes.[34] In terms of charge carrier collection, the SWNTs were originally hypothesized to act as a charge-

selective p-type transport layer which would minimize the formation of a space charge depletion layer at the Au electrode.

The nanohybrid system of P3HT-wrapped SWNTs should act as a selective hole transport layer according to both valence band spectra of x-ray photoelectron spectroscopy (XPS) and UV-Vis absorption spectra. Due to their p-type character, the P3HT-SWNTs provide a more favourable extraction pathway for photogenerated holes from the PbS CQD absorber as opposed to photogenerated electrons. In contrast to the non-selective Au electrode, the SWNT layer should therefore facilitate selective charge extraction, which would result in a reduction of non-radiative recombination at this interface (see figure S6 for a band position diagram). However, fill factor of SWNT was lower than control samples. The factors which can negatively impact device performance, especially fill factor, are the formation of a space charge layer at one of the electrodes due to increased charge carrier recombination,[35,36] reverse saturation current and parasitic resistances.[37] To examine the cause of the charge carrier recombination, measurements of V_{oc} under different white light intensities (figure S5 in supporting information) were carried out. The dependence of V_{oc} to light intensity was regarded to reflect both monomolecular and bimolecular recombination as all of the charges recombine at open-circuit condition.[38] Figure 3a presents the plot of V_{oc} *versus* natural logarithm of the light intensity for both control and SWNT devices. The slope of that plot gives kT/q (where k: Boltzmann constant, T: temperature in Kelvin, and q: elementary charge) for both monomolecular and bimolecular recombination.[39] If monomolecular recombination is influencing in addition to bimolecular recombination, slope greater than kt/q is observed.[40] In figure 3a, SWNT device has shown 2.88kT/q which is bigger than 2.25kT/q from control device. This implies that the imcorporation of SWNT/P3HT allows monocolecular recombination to occur more readily than bimolecular recombination. This

indicates that recombination due to trapping site for either holes or electron has stronger effect with introducing SWNT/P3HT in PMMA layer. The possible trapping site will be at the interface between PbS CQD or P3HT and PMMA matrix which localizes some charge carriers and facilitates the recombination with free charge carriers.

To probe the charge transfer dynamics, we performed ultrafast transient absorption (TA) measurements on samples of 270 nm PbS iodide CQD thin film on the glass with and without the SWNT layer, and PbS CQD film with oleic acid ligands on the glass. These samples were without Au electrodes, and thus optical enhancement caused by light reflected by Au electrodes which will be discussed later, was negligible in these measurements. These measurements should be able to probe the charge transfer kinetics from CQD to SWNT following the light absorption in the CQD layer at picosecond time scales. The samples were pumped with a pulse at 1.55 eV, and probed with a weak probe beam at the energy of the first optical transition peak of PbS CQD (1.30 eV). The probe beam was chosen at 1.30 eV in order to monitor exclusively the electron and hole population at the PbS QDs band edge state, excluding the influence from higher laying states and intraband cooling dynamics. To minimize the influence from the fast dynamics due to multi-exciton recombination, the pump intensity was kept at a low level, such that the average number of absorbed photons per CQD was $\langle N \rangle \approx 0.1 - 0.2$, corresponding to nearly a flux of 10^{22} photons $s^{-1}\,m^{-2}$, which is slightly higher than the photon flux for AM 1.5 (4.3×10^{21} photons $s^{-1}\,m^{-2}$), but still in the low excitation regime. As shown in figure 3b, in this low pump intensity regime, oleic acid (OA) coordinated PbS CQD have extremely long charge carrier relaxation time. An initial small fast decay signal for the OA capped sample is observed and it is fitted to a lifetime of 17 ± 1 ps. This value correspond to the biexciton Auger lifetime for PbS CQDs with band gap at 1.30 eV [41,42], and this is confrmed by pump fluence dependent studies as shown in

the Supplementary Material. When oleic acid is replaced by methylammonium iodide, which is a short chain ligand, the excited carrier may hop to other nanocrystals, as a consequence, the lifetime becomes much shorter. The dynamics may be fitted by a single exponential decay of 210 ± 30 ps (accounting for nearly 85% of the decay), meanwhile the long lived plateau accounts for only about 15% of the signal. . By incorporating the layer of SWNTs on top of the CQD layer, we observe that an even faster component emerges and a bi-exponential decay is necessary to fit the data. to the fastest component is 25 ± 4 ps, accounting for 45% of the decay, while the slow componenet is kept constant, but accounts for only 46% of the amplitude. Meanwhile, the long lived plateau is about 9% of the total dynamics. These results suggest that the fast component is due to fast charge extraction and transport from CQD to SWNT. This reduction in relaxation time in the presence of SWNTs indicates that photogenerated charge carriers are now transferred more rapidly from the CQD films to the SWNT layer. Also, electronic impedance spectroscopy was done for control and SWNT devices which has shown a much lower charge transfer resistance for SWNT device (see figure S10 and table S1 in supporting information). These results further suggests that employing the SWNT-PMMA composite could improve the charge transport throughout the device.

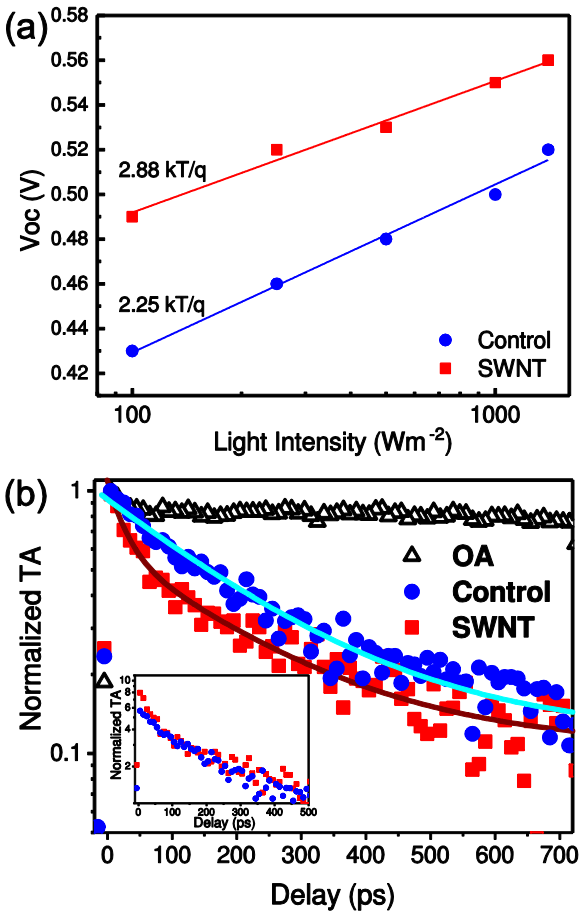

Figure 3. (a) Voc of the control device (without SWNT: red and square symbols) and SWNT device (with SWNT: black and circles symbols) under different illumination intensities. The slope of the linear fitting to Voc versus logarithm of light intensity was analysed as the facor to the thermal voltage. (b) Transient absorption for thin films (270 nm) of PbS CQD capped with oleic acid ligands (OA: open circles, thickness: 200), PbS CQD with iodide ligands (Control: blue circles), and PbS CQD with iodide ligands with SWNT/P3HT (SWNT: red squares). Pump laser for excitation was chosen at 1.55 eV (800 nm) at an estimated photon flux of about 10^{22} photons s^{-1} m^{-2}. The probe was selected to be at the first absorption peak for those samples, ~ 1.30 eV (950 nm).

Optical enhancement

Considering the magnitude of the increase in J_{sc} in the presence of SWNTs, we investigated the impact of the SWNT composite layer on the external quantum efficiency (EQE). Our results from both absorbance and EQE measurements indicate that the inclusion of the composite layer of SWNTs and PMMA enhances the optical absorption and EQE in photovoltaic devices. Figure 4a shows the absorbance spectra for different architectures of the photovoltaic device with Au electrode on top which were made with an integrating sphere. For the device without PMMA and only SWNTs (0 nm in figure 4a), we observe a significant increase in absorbance in a broad region centered around 800 nm with an additional absorption at around 590 nm when compared with the control sample. We attribute this additional peak to the characteristic absorbance feature of the P3HT sheath wrapped around the SWNTs.

In addition to the optical absorption of the SWNTs, the change of the light absorption (absorbance) is also influenced by varying the thickness of PMMA matrix layer (see in figure 4-6). With integrating sphere system, light was illuminated from front ITO glass and pass through devices towards back Au electrodes. As we systematically increase the thickness of the PMMA layer on top of the SWNT layer, we observe a maximum in the absorbance at a thickness of 70 nm (Figure 4a). This corresponds to a rising absorption feature (at around 800 nm) in the EQE spectra, reaching its highest point at 70 nm (Figure 4b). Further increasing the PMMA thickness leads to a re-decrease of the absorptivity and of the EQE feature. This thickness dependence directly translates into Jsc values which reach their maximum value when the absorbance is at its highest and the EQE is at its highest. Interestingly, for PMMA thicknesses beyond 200 nm, we observe a reversal of the trend with a re-increase in photoconversion in the red region of the spectrum. This observation leads us to conclude that the SWNT-PMMA layer acts as an optical

spacer which enhances the absorption properties of the device stack, which contributes to the overall improvement in performance. Optical spacer effects are the result of constructive interference in the absorber layer leading to enhanced light absorption.[43-45] If the extra interface reflects more of the light that has already penetrated the photoactive layer, that helps that photoactive layer to absorb more. The variation of the optical absorbance depending on the thickness of PMMA can be ascribed to the change of the spatial distribution of the light intensity with respect to the absorber layer resulting from the interference between the incident light and reflected light from the electrode. By varying the thickness of PMMA, the intensity of the interference occurs at different depths of the PbS photoactive layer. At a PMMA thickness of 70 nm, the intensity peak appears to be optimally located inside the absorber allowing for maximal photoconversion.

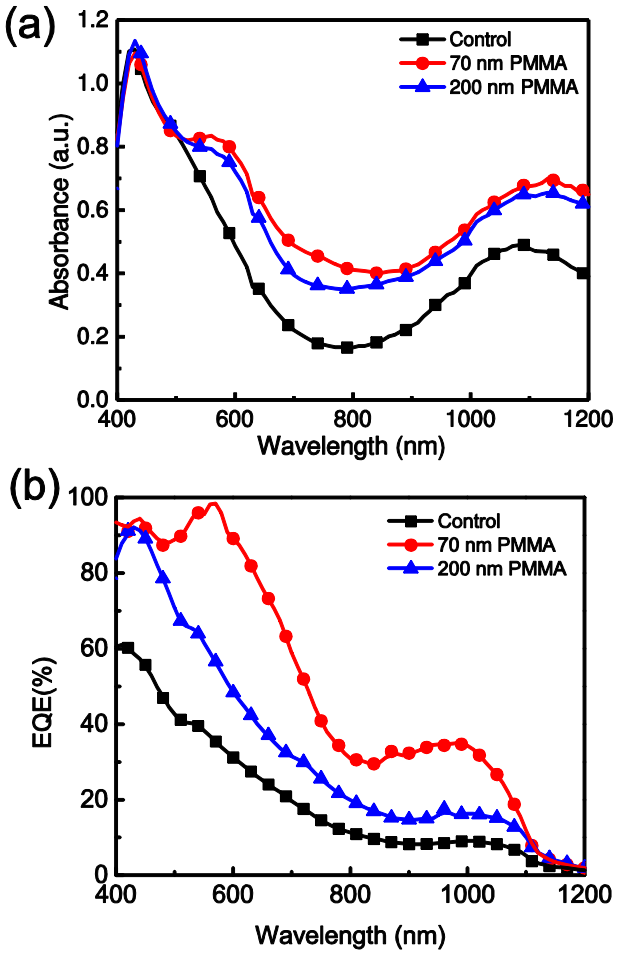

Figure 4. (a) Absorbance of control (black square symbols) without both SWNT/P3HT and PMMA, 70 nm (SWNT with 70 nm PMMA matrix) device (red circle symbols), and 200 nm (SWNT with 200 nm PMMA matrix) device (blue triangle symbols). (b) External quantum efficiencies (EQE) for control (black square symbols), 70 nm (SWNT with 70 nm PMMA matrix) device (red circle symbols), and 200 nm (SWNT with 200 nm PMMA matrix) device (blue triangle symbols) with a light from 400 nm to 1200 nm.

To support this hypothesis, we modeled the effect of the PMMA layer thickness on the current generation employing a transfer-matrix formalism developed by Burkhard *et al.*.[46] The optical constants for the PbS layer required for the model were first measured by ellipsometry. In this modeling approach we investigate how the photocurrent generation in the device stack is affected by a variations of the PMMA layer thickness. To simplify the approach we assume an internal quantum efficiency of 100%. The resulting current dependence on the PMMA layer

thickness (Figure S9) follows the experimental trend (Figure 7)), as there is a clear maximum at around 50 nm, and a minimum at around 200 nm. Modelling the absorption through the device stack shows that the stack with 50 nm PMMA, has an increased absorption peak between 900 and 1000 nm, which is in good agreement with the increased EQE in the same range (Figure 4 b)). In fact, by modeling the electric field intensity of the light through the device stack for different wavelengths (Figure S11), we can show that the addition of 50 nm of PMMA, has a strong effect especially on the 1000 nm wavelengths. In contrast to the stack without PMMA, a much higher fraction of the field distribution conincides with the CQD absorber layer of the stack at this wavelength resulting in an increase in charge generation (Figure S12). Similarly, we observe that a larger fraction of the electric field at 600 nm conincides with the absorber layer, which is consistent with the enhanced EQE measured at this wavelength (Figure 4b).

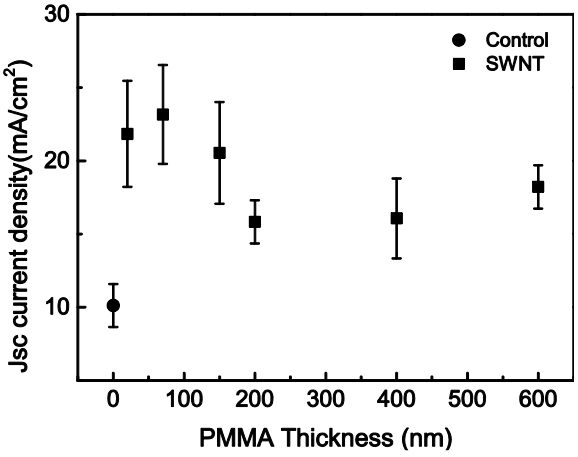

Figure 5. Comparison of Jsc among control device and SWNT devices. The thickness of PMMA were varied, and 0 nm, 20 nm, 70 nm, 150 nm, 200 nm, 400 nm, 600 nm for those SWNT devices.

The overall comparisons of the obtained data from absorbance measurement and EQE measurement were summarized in figure 6. As shown in this figure, the absorption traces were reflected in the EQE results except for the SWNT device with 70 nm of PMMA (70 nm SWNT

device) and the one with 400 nm of PMMA (400 nm SWNT device). For 70 nm SWNT device, EQE signal was exceptionally high in NIR region (800-1100 nm) compared to the other device with different PMMA thickness. This can be ascribed to the depth where NIR absorption occurs in PbS CQD thin film. If the peak of the interfered light happens to be at the optimal depth in the device stack regarding the lifetime and diffusion length of minority carrier, the quantum efficiency would rise. Next, although the absorbance data shows that 400 nm SWNT device had the analogous spectrum to SWNT device with 600 nm PMMA (600 nm SWNT device) matrix, EQE of former was lower than the one of latter in short-wavelength region. The cause of this mismatch between absorbance data and EQE data might be the carrier recombination happening at the functional layer. The series resistance of 400 nm SWNT device was significantly low (18 Ω cm^2) compared to one of different device architectures (see figure S8b). This series resistance value of 400 nm SWNT device suggests that the carrier recombination happens the most because of the resistance in SWNT/P3HT-PMMA layer with exceptionally thick PMMA matrix. The difference of series resistance and EQE between 400 nm SWNT device and 600 nm SWNT device might be just merely the morphological deviation of SWNT/P3HT in the solution processing.

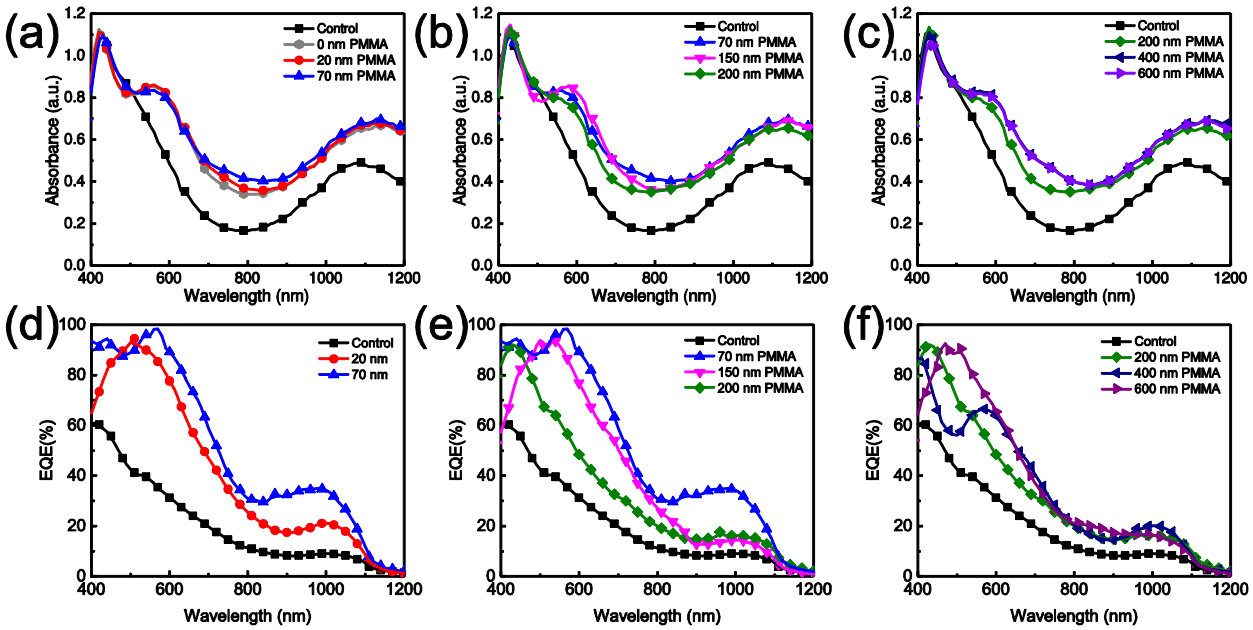

Figure 6. Absorbance of (a) a set of full control stack without both SWNT/P3HT and PMMA, 0 nm (SWNT without PMMA matrix) device, 20 nm (SWNT with 20 nm PMMA matrix) device, and 70 nm (SWNT with 70 nm PMMA matrix) device, (b) a set of control, 70 nm device, 150 nm device, and 200 nm device, and (c) a set of control, 200 nm device, 400 nm device, and 600 nm device. EQE of (d) a set of control without both SWNT/P3HT and PMMA, 0 nm (SWNT without PMMA matrix) device, 20 nm (SWNT with 20 nm PMMA matrix) device, and 70 nm (SWNT with 70 nm PMMA matrix), (e) a set of EQE of control, 70 nm device, 150 nm device, and 200 nm device, and (f) a set of EQE of control, 200 nm device, 400 nm device, and 600 nm device.

This transfer-matrix model provides strong support for the optical spacer effect by matching the observed experimental trends with theoretical predictions of absorption and charge generation. Quantitatively, the experimental trends exceed these predictions to some extent which can be explained by taking into consideration the previous observations of enhanced hole transfer due to the presence of the SWNTs, which significantly enhance the effect of the optical spacer. This is well illustrated by the comparison of the device stack without SWNTs or PMMA, and the device stack with SWNTs and 70 nm PMMA, which results in a significant increase in photocurrent extraction. The model predicts that the addition of a PMMA layer of this thickness should more than double the charge generation near the p-type interface (Figure S11). The

increase in J_{sc} is therefore probably the result of compounding positive effects of improved charge transport, increased photoconversion and vicinity of charge generation.

Stability

In addition to improving the overall device performance, we also find that the SWNT-PMMA layer enhances the device stability. This observation is confirmed by tracking the device performance over a 35-day period, where the devices were stored in ambient air without humidity control under dark condition (see figure 7). Although some deterioration of the performance can be observed for the SWNT devices, they appear to retain the majority of their initial efficiency, while the control devices perform almost 50% worse than initially by 35 days. The way to store devices under dark condition is comparable with ISOS-D-1 according to the stability testing protocols for organic PV.[47]

Our hypothesis is that the protective effect of the PMMA layer which blocks the ingress of water and oxygen which could degrade the quality of the photoactive PbS CQD layer by affecting the surface defects of the nanocrystals and ligands coordinating to the nanocrystals. The oxidized surface defects on nanocrystals create mid-gap states which facilitate charge carrier recombination,[48] or change the electronic structure and the position of the energy levels of a CQD thin film.[49] This energy level alteration can explain the trends of Voc in control devices. Some extent of oxidation in the photovoltaics was found to improve the band alignment of the photovoltaics,[50] and it could be due to the improvement of Voc after 10 days of the storage. However, further oxidation of PbS made Voc deteriotated after that day. The alteration of the electronic energy levels of the PbS CQD layer can generate a potential barrier at the interface

with the cathode or the n-type semiconductor causing a loss in potential or a decrease in charge extraction.

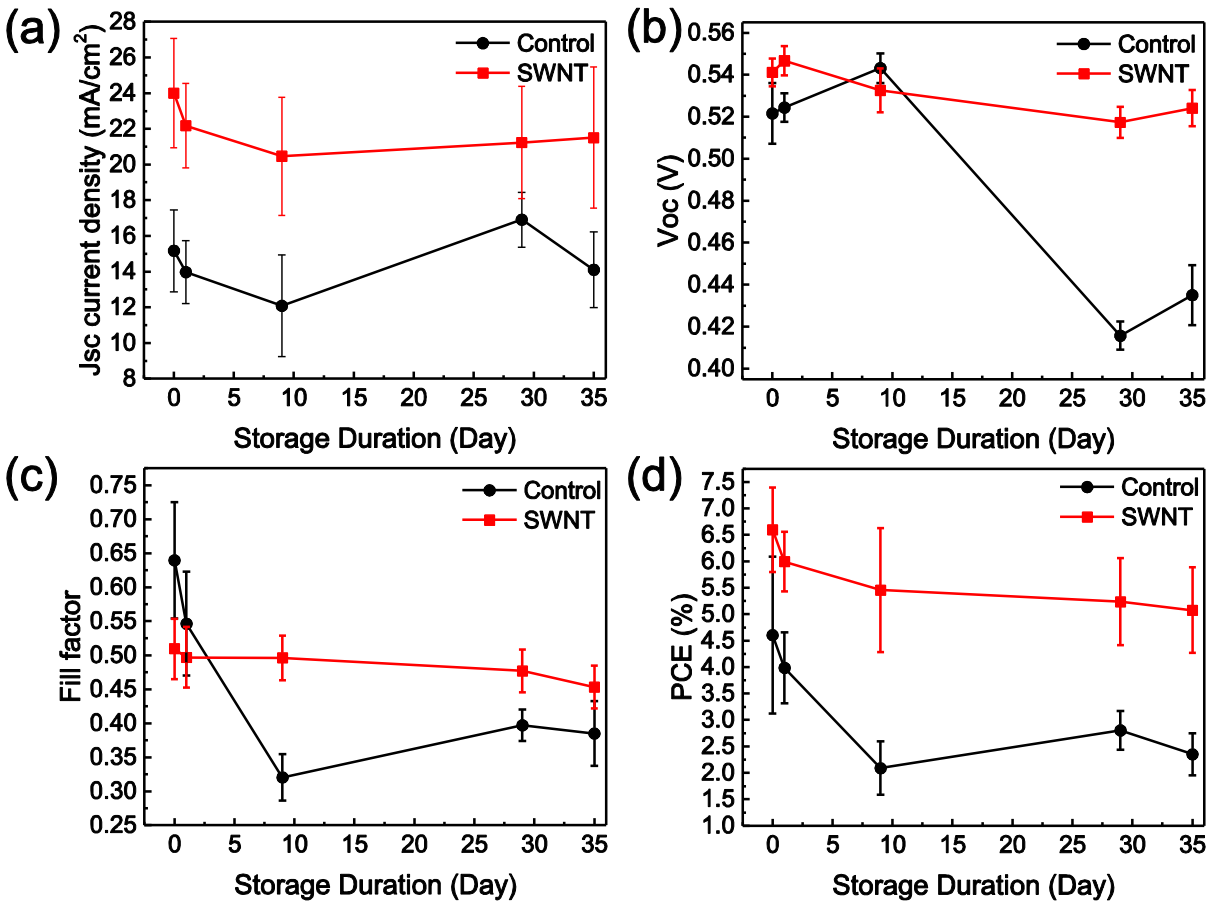

Figure 7. The variation of photovoltaic performance metrics of devices, with and without SWNT/P3HT-PMMA, with storage time. **(**a) J_{sc}, (b) V_{oc}, (c) FF, and (d) PCE. The devices were unencapsulated and were stored in the ambient air between each measurements in a dark environment without any humidity control. The standard deviation (error bars) and the average (data point) were calculated from a sample of 12 devices on 4 separate substrates.

CONCLUSION

By employing SWNTs in a PMMA matrix as a hole extraction layer between the photoactive PbS CQD thin film and the Au back electrode, we demonstrate an improvement of up to 50% for the photocurrent of such CQD devices, which results in a significant enhancement of the overall power-conversion efficiency.

We provide experimental and theoretical evidence that the increase in photocurrent comes from an optical enhancements in the device with a faster carrier transfer, namely enhanced light management and better hole extraction. The latter results from the PMMA layer acting as an optical spacer leading to a significant boost of the external quantum efficiency of the PbS CQD absorber.

Furthermore, ultrafast transient absorption measurements suggest much faster hole transfer in the presence of the SWNT-PMMA layer. In fact, we propose that the improvement in the charge-transport characteristics by the SWNTs lead to hole-dominant charge extraction which, in turn, results in the formation of a space charge region causing increased non-radiative charge carrier recombination and thus an overall lower fill factor. In future studies, we will focus on improving the charge carrier concentration and mobility in the n-type semiconductor to be able to compete with the highly p-type SWNTs, to achieve more balanced charge transport, and thus higher performance.

Table 1. The comparison of control device and SWNT device in relaxation time in transient absorption (ps), J_{sc} (mA cm^{-2}), Voc (V), fill factor, and power conversion efficiency (%).

device	relaxation time in transient absorption (ps)	J_{sc} (mA cm^{-2})	V_{oc}(V)	FF	PCE (%)
control	81 ± 9	14.0 ± 1.77	0.52 ± 0.00(7)	0.54 ± 0.07	3.99 ± 0.67
SWNT	36 ± 6	22.2 ± 2.38	0.55 ± 0.00(7)	0.49 ± 0.04	5.99 ± 0.56

METHODS

Synthesis of PbS colloidal quantum dots. 2.1 mmol lead (II) oxide (99.0 % from Sigma-Aldrich), 5.7 mmol of oleic acid (technical grade 90 % from Sigma-Aldrich) were mixed in 10 g of 1-octadecene (technical grade 90 % from Sigma-Aldrich) for at least 2 hours at 90 °C under vacuum to obtain lead oleate complexes as a lead precursors. After setting solution temperature to 105 °C, 1 mmol bis(trimethylsilyl) sulfide in 5 g 1-octadecene was injected followed by the ambient air cooling to room temperature. CQDs were purified by adding acetone, followed by centrifugation. The extracted CQDs were re-dispersed in hexane and were further precipitated twice with methanol, and then finally dispersed in octane 50 mg mL^{-1}.

Synthesis of ZnO nanoparticles. ZnO nanocrystals were synthesized by using the method according to Womelsdorf *et al.*.[51] 13.4 mmol of zinc acetate dihydrate was dissolved in 125 mL of methanol, and 26.9 mmol of potassium hydroxide was dissolved in 65 mL of methanol with stirring at 60 ºC. Then, potassium hydroxide solution was added dropwise to zinc acetate solution, and solution mixture was under stirring at 60 ºC for 2.5 h. Yielded ZnO nanoparticles were treated in purification by methanol with centrifugation and decantation twice. Finally, a mixture of 5 mL of chloroform and 5 mL of methanol was added to dissolve the precipitation.

Solution-phase ligand Exchange. This ligand exchange is following the method reported by Ning *et al.*.[52] 0.8 mL of 50 mg mL^{-1} PbS CQD in octane solution has been diluted in 4 mL of 10 mg mL^{-1} solution. The diluted solution was vigorously mixed with 5mL of 0.63 M methylammonium iodide (from Dyesol) solution in N,N-dimethylformamide (DMF) (99.8 % from Sigma-Aldrich). After PbS nanocrystals moved from octane phase to DMF phase, solution was washed with octane three times. After decantation, 0.2 mL of toluene was added to precipitate CQDs. After 6000 rpm centrifugation for 10 mins, supernatant was decanted and

precipitates were dried under N_2 atmosphere. Precipitated PbS CQDs were dissolved in 160 μL butylamine.

Solar cell fabrication. After the cleaning by 45 ºC dilstiled water with 2 % Decon 90, distilled water, acetone, and IPA in the ultrasonicator for 15 mins. under 50 °C, and drying of glass substrates (11 mm×14 mm) spattered with ITO (Präzisions Glas & Optik CEC010S), ZnO nanoparticles were deposited on them by spin-coating (2000 rpm for 30 secs). After annealing of substrates for 10 mins at 100 ºC, prepared PbS solution in butylamine was spun-coat on these substrates for 90 secs at 2500 rpm in the ambient condition. 200 μL of 0.12 mg mL^{-1} SWNT/P3HT solution in chloroform, which has been functionalized by following method presented in Habisreutinger *et al.*,[53] was deposited on substrates dropwise at dispense rate of 3000 rpm immediately followed by a spin-coating of 20 mg mL^{-1} PMMA in chlorobenzene solution in the ambient air. SWNTs were purchased from Unidym, and rr-P3HT was purchased from Rieke Metals Inc.. The thicknesses of PbS CQD thin films and PMMA matrices layer were determined by Dektak stylus profiler (Bruker). 100 nm Au was evaporated on top of substrates with a mask (rate: 0.1-0.2 nm/s, base pressure: 1×10^{-5} Torr) for making three Au strips (width: 1.43 mm) on a substrate.

Device characterisation. All solar cell devices were loaded into a sealed testing chamber with N_2 purged through testing. There were 12 devices fabricated and tested for both control and SWNT device structure respectively. Current−voltage (J−V) curves were measured using a Keithley 2400 Source Meter. The voltage was swept from -0.4 V to 1.0 V with a step of 0.033 V with the scanning speed of 100 ms/step. AM 1.5 solar spectrum illumination was produced by an Abet Technologies model 11002 Solar Simulator with an AM 1.5G filter. The power density of the light source was calibrated with a Si reference cell from Abet Technologies. EQE was tested

with the Oriel 1/8 m monochromator from Newport. 410 nm, 600 nm, and 1000 nm filters were used to gain corresponding EQE curves. Photodiode sensors (818-UV and 918-IR) from Newport were used to calibrate the power. To avoid overestimation of performance due to edge effects, a mask (1.00 mm^2) that is smaller than the actual geometric overlap area of the cathode and anode (2.04 mm^2) was used when testing the I-V curves.

Electron microscopy. Transmission Electron Microscopy (TEM) analysis was performed on a JEOL-JEM 2100 LaB6 microscope with an information limit of 0.16 nm at an accelerating voltage of 200 kV. Samples were prepared by drop-casting nanotube dispersions onto lacey carbon film-coated copper grids. Scanning electron Microscope (SEM) imaging was performed using a Zeiss Nvision 40 FIB-SEM. Sample preparation for cross sectioning involved securing the glass substrate to a 12mm stub using carbon tape, followed by grounding the top contacts to the stub using conductive silver paint. To preserve the gold top-contact, e-beam deposition was performed prior to ion milling. Under a reduced raster from the scanning electron beam (5kV power, 120µm aperture, high current mode), a stream of carbon gas was passed over the sample for 5 minutes. The cross section was milled with a 30kW/80pA Ga+ ion beam to a depth of 1µm. Images were taken using a secondary electron detector at 3kV using a 30µm aperture, with the sample tilted to 36° from the normal.

Transient Absorption. Transient absorption has been performed using an amplified Ti:sapphire laser system operating at 1 kHz with pulses of about 100 fs. The excitation pulse was chosen at 800 nm (1.55 eV), while the probe pulse was selected from an optical parametric amplifier at 930 nm (1.33 eV), keeping its intensity about 10 times lower than the excitation pulse. To avoid multi-exciton interactions, which could influence our data analysis, the excitation intensity was

chosen such that the average number of absorbed photon per nanomaterial is much less than 1. The samples were deposited on the SiO_2 glass.

Spectroscopic Ellipsometry. Spectroscopic ellipsometry data (measured at angles 45, 55 and 65 degrees) of CQD thin film (at thickness 160 nm) and PMMA films (at thickness 205 nm) were measured using Woollam RC2 Spectroscopic Ellipsometer (210 nm - 1700 nm). Data analysis for thickness and refractive indices was carried out in CompleteEASE software provided with the instrument. These derived values were utilized for simulation modelling.

ACKNOWLEDGMENT

Y.Tazawa acknowledges for the financial support from Japan Student Services organization (L14326150008). L.A.Padilha and A.A.R.Watt acknowledge the Royal Society – Newton Advanced Fellowship (NA 150152). G.Nagamine and L.A.Padilha acknowledge the financial support from FAPESP (2013/16911-2). The work was also supported by the International Collaborative Energy Technology R&D Program of the Korean Institute of Energy Technology Evaluation and Planning (KETEP) with financial resource from the Ministry of Trade, Industry & Energy, Republic of Korea (No. 20148520011250). M.Riede acknowledges funding from EC FP 7 MSCA - Career Integration Grant (630864) and EPSRC (EP/M015173/1). G.Mazzotta acknowledges funding throught the EPSRC CDT Plastic Electronics (EP/L01551X/1) and University College, Oxford.

ASSOCIATED CONTENT

Supporting Information

It has following contents: FT-IR with ligand exchange of PbS colloidal quantum dots, optical characteristics of functional layers, further experimental details about J-V curve measurement, parasitic resistance, cyclic voltammograms, and further detail about the influence of the variation of PMMA thickness to optical absorption and EQE. This material is available free of charge *via* the internet at http://pubs.acs.org.

AUTHOR INFORMATION

Corresponding Author

*E-mail: andrew.watt@materials.ox.ac.uk. Tel.: +44 1865 613455 or +44 7828 598301. Fax.: +44 1865 273789 (A.A.R.W.).

Author Contributions

The manuscript was written through contribution by each author categorized into following roles. Tazawa, Y. established the study conception, methodology, performed the device fabrication and general characterization, curated data, and wrote the initial draft. Habisreutinger, S.N. established the study conception, methodology for the modelling of optical distribution, and supplied of single-walled carbon nanotubes solution. Zhang, N. contributed to this project by his critical review, commentary or revision to the manuscript. Gregory, D.A.F. took a FIB-SEM micrograph of photovoltaic device. Nagamine, G. performed transient absorption measurement. Kesava, S.V. performed ellipsometry for the optical modeling combined with AFM data. Mazzotta, G. performed AFM for the optical modeling combined with ellipsometry data. Riede, M. contributed to this project through his critical review, study conception for the determination and measurement of the optical interference pattern, commentary and revision of the manuscript, and funding acquisition. Padilha, L.A. established the methodology and formal analysis for transient absorption. Nicholas, R.J. contributed to this project by establishing the study conception, giving the critical review, commentary and revision to the manuscript, and acquiring the funding. Watt, A.A.R. contributed to this project by project administration, study conception, supervision, and funding acquisition

Notes

The authors declare no competing financial interest.

REFERENCES

(1) Kramer, I. J.; Minor, J. C.; Moreno-Bautista, G.; Rollny, L.; Kanjanaboos, P.; Kopilovic, D.; Thon, S. M.; Carey, G. H.; Chou, K. W.; Zhitomirsky, D. *et al.* Efficient Spray-Coated Colloidal Quantum Dot Solar Cells. *Adv. Mater.* **2015**, *27*, 116–121.

(2) Luther, J. M.; Law, M.; Beard, M. C.; Song, Q.; Reese, M. O.; Ellingson, R. J.; Nozik, A. J. Schottky Solar Cells Based on Colloidal Nanocrystal Films. *Nano Lett.* **2008**, *8*, 3488–3492.

(3) Murphy, J. E.; Beard, M. C.; Norman, A. G.; Ahrenkiel, S. P.; Johnson, J. C.; Yu, P.; Mićić, O. I.; Ellingson, R. J.; Nozik A. J. PbTe Colloidal Nanocrystals: Synthesis, Characterization, and Multiple Exciton Generation. *J. Am. Chem. Soc.* **2006**, 128, 3241–3247.

(4) Shabaev, A.; Efros, A. L.; Nozik, A. J. Multiexciton Generation by a Single Photon in Nanocrystals. *Nano Lett.* **2006**, *6*, 2856–2863.

(5) Alivisatos, A. P. Semiconductor Clusters, Nanocrystals, and Quantum Dots. *Science* **1996**, *271*, 933–937.

(6) Brown, P. R.; Kim, D.; Lunt, R. R.; Zhao, N.; Bawendi, M. G.; Grossman, J. C.; Bulović, V. Energy Level Modification in Lead Sulfide Quantum Dot Thin Films Through Ligand Exchange. *ACS Nano* **2014**, *8*, 5863–5872.

(7) Luther, J. M.; Law, M.; Song, Q.; Perkins, C. L.; Beard, M. C.; Nozik, A. J. Structural, Optical, and Electrical Properties of Self-Assembled Films of PbSe Nanocrystals Treated with 1, 2-Ethanedithiol. *ACS Nano* **2008**, *2*, 271–280.

(8) Tang, J.; Kemp, K. W.; Hoogland, S.; Jeong, K. S.; Liu, H.; Levina, L.; Furukawa, M.; Wang, X.; Debnath, R.; Cha, D. *et al.* Colloidal-Quantum-Dot Photovoltaics Using Atomic-Ligand Passivation. *Nat. Mater.* **2011**, *10*, 765–771.

(9) Zhang, J.; Gao, J.; Miller, E. M.; Luther, J. M.; Beard, M. C. Diffusion-Controlled Synthesis of PbS and PbSe Quantum Dots with In Situ Halide Passivation for Quantum Dot Solar Cells. *ACS Nano* **2014**, *8*, 614–622.

(10) Balazs, D. M.; Dirin, D. N.; Fang, H.-H.; Protesescu, L.; ten Brink, G. H.; Kooi, B. J.; Kovalenko, M. V.; Loi, M. A. Counterion-Mediated Ligand Exchange for PbS Colloidal Quantum Dot Superlattices. *ACS Nano* **2015**, *9*, 11951–11959.

(11) Chuang, C. H. M.; Brown, P. R.; Bulović, V.; Bawendi, M. G. Improved Performance and Stability in Quantum Dot Solar Cells Through Band Alignment Engineering. *Nat. Mater.* **2014**, *13*, 796–801.

(12) Chuang, C. H. M.; Maurano, A.; Brandt, R. E.; Hwang, G. W.; Jean, J.; Buonassisi, T.; Bulović, V.; Bawendi, M. G. Open-Circuit Voltage Deficit, Radiative Sub-Bandgap States, and prospects in Quantum Dot Solar Cells. *Nano Lett.* **2015**, *15*, 3286–3294.

(13) Tress, W.; Leo, K.; Riede, M. Influence of Hole-Transport Layers and Donor Materials on Open-Circuit Voltage and Shape of I-V Curves of Organic Solar Cells. *Adv. Funct. Mater.* **2011**, *21*, 2140–2149.

(14) Bi, D.; Yang, L.; Boschloo, G.; Hagfeldt, A.; Johansson, E. M. J. Effect of Different Hole

Transport Materials on Recombination in CH3NH3PbI3 Perovskite-Sensitized Mesoscopic Solar Cells. *J. Phys. Chem. Lett.* **2013**, *4*, 1532–1536.

(15) Snaith, H. J. Perovskites: The Emergence of a New Era for Low-Cost, High-Efficiency Solar Cells. *J. Phys. Chem. Lett.* **2013**, *4*, 3623–3630.

(16) Lattante, S. Electron and Hole Transport Layers: Their Use in Inverted Bulk Heterojunction Polymer Solar Cells. *Electronics* **2014**, *3*, 132–164.

(17) Willis, S. M.; Cheng, C.; Assender, H. E.; Watt, A. A. R. The Transitional Heterojunction Behavior of PbS/ZnO Colloidal Quantum Dot Solar Cells. *Nano Lett.* **2012**, *12*, 1522–1526.

(18) Marinova, N.; Tress, W.; Humphry-Baker, R.; Dar, M. I.; Bojinov, V.; Zakeeruddin, S. M.; Nazeeruddin, M. K.; Gratzel, M. Light¨ Harvesting and Charge Recombination in $CH_3NH_3PbI_3$ Perovskite Solar Cells Studied by Hole Transport Layer Thickness Variation. ACS Nano **2015**, 9 (4), 4200−4209

(19) National Renewable Energy Laboratory Research Cell Efficiency Records http://www.nrel.gov/ncpv/images/efficiency_chart.jpg (accessed Feb 27, 2017).

(20) Ehrler, B.; Musselman, K. P.; Böhm, M. L.; Morgenstern, F. S. F.; Vaynzof, Y.; Walker, B. J.; MacManus-Driscoll, J. L.; Greenham, N. C. Preventing Interfacial Recombination in Colloidal Quantum Dot Solar Cells by Doping the Metal Oxide. *ACS Nano* **2013**, *7*, 4210–4220.

(21) Roy, A.; Park, S. H.; Cowan, S.; Tong, M. H.; Cho, S.; Lee, K.; Heeger, A. J. Titanium Suboxide as an Optical Spacer in Polymer Solar Cells. *Appl. Phys. Lett.* **2009**, *95*, 13302.

(22) Kim, J. Y.; Kim, S. H.; Lee, H. H.; Lee, K.; Ma, W.; Gong, X.; Heeger, A. J. *Adv. Mater.* **2006**, *18* (5), 572–576.

(23) Kim, J. Y.; Kim, S. H.; Lee, H.-H.; Lee, K.; Ma, W.; Gong, X.; Heeger, A. J. New Architecture for High-Efficiency Polymer Photovoltaic Cells Using Solution-Based Titanium Oxide as an Optical Spacer. *Adv. Mater.* **2006**, *18*, 572–576.

(24) Ajayan, P. M. Nanotubes from Carbon. *Chem. Rev.* **1999**, *99*, 1787–1800.

(25) Dürkop, T.; Getty, S. A.; Cobas, E.; Fuhrer, M. S. Extraordinary Mobility in Semiconducting Carbon Nanotubes. *Nano Lett.* **2004**, *4*, 35–39.

(26) Javey, A.; Guo, J.; Wang, Q.; Lundstrom, M.; Dai, H. Ballistic Carbon Nanotube Field-Effect Transistors. *Nature* **2003**, *424*, 654–657.

(27) Lieber, C. M.; Odom, T. W.; Huang, J.-L.; Kim, P. Atomic Structure and Electronic Properties of Single-Walled Carbon Nanotubes. *Nature* **1998**, *391*, 62–64.

(28) Wilder, J. W. G.; Venema, L. C.; Rinzler, A. G.; Smalley, R. E.; Dekker, C. Electronic Structure of Atomically Resolved Carbon Nanotubes. *Nature* **1998**, *391*, 59–62.

(29) Dabera, G. D. M. R.; Jayawardena, K. D. G. I.; Prabhath, M. R. R.; Yahya, I.; Tan, Y. Y.; Nismy, N. A.; Shiozawa, H.; Sauer, M.; Ruiz-Soria, G.; Ayala, P. *et al.* Hybrid carbon nanotube networks as efficient hole extraction layers for organic photovoltaics. *ACS Nano* **2013**, *7* (1), 556–565.

(30) Habisreutinger, S. N.; Leijtens, T.; Eperon, G. E.; Stranks, S. D.; Nicholas, R. J.; Snaith, H. J. Enhanced Hole Extraction in Perovskite Solar Cells Through Carbon Nanotubes. *J.*

Phys. Chem. Lett. **2014**, *5* (23), 4207–4212.

(31) Habisreutinger, S. N.; Wenger, B.; Snaith, H. J.; Nicholas, R. J. Dopant-Free Planar n–i–p Perovskite Solar Cells with Steady-State Efficiencies Exceeding 18%. *ACS Energy Lett.* **2017**, *2* (3), 622–628.

(32) Habisreutinger, S. N.; Nicholas, R. J.; Snaith, H. J. Carbon Nanotubes in Perovskite Solar Cells. *Adv. Energy Mater.* **2017**, *7* (10), 1601839.

(33) Pacholski, C.; Kornowski, A.; Weller, H. Self-Assembly of ZnO: From Nanodots to Nanorods. *Angew. Chemie Int. Ed.* **2002**, *41*, 1188–1191.

(34) Würfel, U. Limitation of Energy Conversion in Solar Cells. In *Physics of Solar Cells: From Basic Principles to Advanced Concepts*; Würfel, P.; John Wiley & Sons: Weinheim, 2016; pp 168.

(35) Sah, C.; Noyce, R.; Shockley, W. Carrier Generation and Recombination in P-N Junctions and P-N Junction Characteristics. *Proc. IRE* **1957**, *45*, 1228–1243.

(36) Mauer, R.; Howard, I. A.; Laquai, F. Effect of Nongeminate Recombination on Fill Factor in Polythiophene/Methanofullerene Organic Solar Cells. *J. Phys. Chem. Lett*. **2010**, *1*, 3500–3505.

(37) Jha, A. R. Classification of Solar Cells Based on Performance, Design Complexity, and Manufacturing Costs. In *Solar Cell Technology and Applications*; Jha, A. R.; CRC Press: New York, 2009; pp 94

(38) Kyaw, A. K. K.; Wang, D. H.; Gupta, V.; Leong, W. L.; Ke, L.; Bazan, G. C.; Heeger, A. J. Intensity Dependence of Current–Voltage Characteristics and Recombination in High-Efficiency Solution-Processed Small-Molecule Solar Cells. *ACS Nano* **2013**, *7*, 4569–4577.

(39) Wetzelaer, G. A. H.; Kuik, M.; Lenes, M.; Blom, P. W. M. Origin of the Dark-Current Ideality Factor in Polymer:fullerene Bulk Heterojunction Solar Cells. *Appl. Phys. Lett.* **2011**, *99*, 153506.

(40) Mandoc, M. M.; Veurman, W.; Koster, L. J. A.; de Boer, B.; Blom, P. W. M. Origin of the Reduced Fill Factor and Photocurrent in MDMO-PPV:PCNEPV All-Polymer Solar Cells. *Adv. Funct. Mater.* **2007**, *17*, 2167–2173.

(41) Padilha, L. A.; Stewart, J. T.; Sandberg, R. L.; Bae, W. K.; Koh, W.-K.; Pietryga, J. M.; Klimov, V. I. Carrier Multiplication in Semiconductor Nanocrystals: Influence of Size, Shape, and Composition. *Acc. Chem. Res.* **2013**, *46*, 1261–1269.

(42) Stewart, J. T.; Padilha, L. A.; Qazilbash, M. M.; Pietryga, J. M.; Midgett, A. G.; Luther, J. M.; Beard, M. C.; Nozik, A. J.; Klimov, V. I. Comparison of Carrier Multiplication Yields in PbS and PbSe Nanocrystals: The Role of Competing Energy-Loss Processes. *Nano Lett.* **2012**, *12*, 622–628.

(43) Gilot, J.; Barbu, I.; Wienk, M. M.; Janssen, R. A. J. The Use of ZnO as Optical Spacer in Polymer Solar Cells: Theoretical and Experimental Study. *Appl. Phys. Lett.* **2007**, *91*, 113520.

(44) Andersson, B. V.; Persson, N.-K.; Inganäs, O. Comparative Study of Organic Thin Film Tandem Solar Cells in Alternative Geometries. *J. Appl. Phys.* **2008**, *104*, 124508.

(45) Kyaw, A. K. K.; Wang, D. H.; Wynands, D.; Zhang, J.; Nguyen, T.-Q.; Bazan, G. C.; Heeger, A. J. Improved Light Harvesting and Improved Efficiency by Insertion of an Optical Spacer (ZnO) in Solution-Processed Small-Molecule Solar Cells. *Nano Lett.* **2013**, *13*, 3796–3801.

(46) Burkhard, G. F.; Hoke, E. T.; McGehee, M. D. *Adv. Mater.* **2010**, *22* (30), 3293–3297.

(47) Reese, M. O.; Gevorgyan, S. A.; Jørgensen, M.; Bundgaard, E.; Kurtz, S. R.; Ginley, D. S.; Olson, D. C.; Lloyd, M. T.; Morvillo, P.; Katz, E. A. *et al.* Consensus Stability Testing Protocols for Organic Photovoltaic Materials and Devices. *Sol. Energy Mater. Sol. Cells* **2011**, *95*, 1253–1267.

(48) Ip, A. H.; Thon, S. M.; Hoogland, S.; Voznyy, O.; Zhitomirsky, D.; Debnath, R.; Levina, L.; Rollny, L. R.; Carey, G. H.; Fischer, A. *et al.* Hybrid Passivated Colloidal Quantum Dot Solids. *Nat. Nanotechnol.* **2012**, *7*, 577–582.

(49) Chang, J.; Kuga, Y.; Mora-Seró, I.; Toyoda, T.; Ogomi, Y.; Hayase, S.; Bisquert, J.; Shen, Q. High Reduction of Interfacial Charge Recombination in Colloidal Quantum Dot Solar Cells by Metal Oxide Surface Passivation. *Nanoscale* **2015**, *7*, 5446–5456.

(50) Neo, D. C. J.; Zhang, N.; Tazawa, Y.; Jiang, H.; Hughes, G. M.; Grovenor, C. R. M.; Assender, H. E.; Watt, A. A. R. Poly(3-hexylthiophene-2, 5-diyl) as a Hole Transport Layer for Colloidal Quantum Dot Solar Cells. *ACS Appl. Mater. Interfaces* **2016**, *8*, 12101–12108.

(51) Womelsdorf, H.; Hoheisel, W.; Passing, G. Nanoparticulate, Redispersible Zinc Oxide Gels. U.S. Patent 6,710,091, August 31, 2000.

(52) Ning, Z.; Dong, H.; Zhang, Q.; Voznyy, O.; Sargent, E. H. Solar Cells Based on Inks of n-type Colloidal Quantum Dots. *ACS Nano* **2014**, *8*, 10321–10327.

(53) Habisreutinger, S. N.; Leijtens, T.; Eperon, G. E.; Stranks, S. D.; Nicholas, R. J.; Snaith, H. J. Carbon Nanotube/Polymer Composites as a Highly Stable Hole Collection Layer in Perovskite Solar Cells. *Nano Lett.* **2014**, *14*, 5561–5568.

For Table of Contents Use Only

Carbon Nanotubes for Quantum Dot Photovoltaics with Enhanced Light Management and Charge Transport

Yujiro Tazawa, Severin N. Habisreutinger, Nanlin Zhang, Daniel A.F. Gregory, Gabriel Nagamine, Sameer V. Kesava, Giulio Mazzotta, Moritz Riede, Lazaro A. Padilha, Robin J. Nicholas, Andrew A.R. Watt

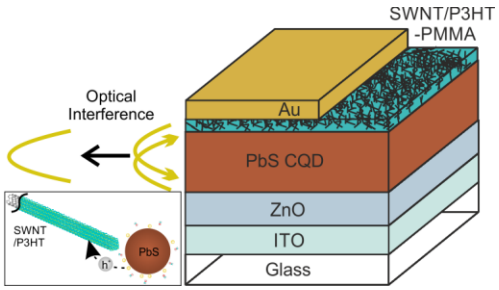

Table of Contents: This figure illustrates that an optical interference enhances the light absorption in a PbS CQD layer in PbS CQD photovoltaic devices with the SWNT/P3HT in PMMA matrix layer. In addition, the small schematic is indicating that a hole is transported from PbS CQD to SWNT/P3HT.